Indian Journal of Pure & Applied Physics
Vol. 63, May 2025, pp. 427-438
DOI: 10.56042/ijpap.v63i5.17297

High-Efficiency $BaZrS_3$ and $BaZrSe_3$ Chalcogenide Perovskite Solar Cells: A Numerical Optimization Study

Nikhil Thakur[a*], Pankaj Sharma[b] & Pawan Kumar[a]

[a]School of Physics and Materials Science, Shoolini University, Solan 173 229, India

[b]Applied Science Department, National Institute of Technical Teachers Training and Research, Chandigarh 160 019, India

Received: 20 March 2025; accepted: 21 April 2025

Chalcogenide perovskites (CPs) have emerged as promising alternatives to lead halide perovskites due to their superior optoelectronic properties, stability, and nontoxicity. Among these, $BaZrS_3$ and $BaZrSe_3$ has garnered significant interest for photovoltaic applications, thanks to its excellent light absorption capabilities and environmental friendliness. In this study, the performance of $BaZrS_3$ and $BaZrSe_3$-based solar cells was numerically simulated and optimized using SCAPS-1D (version 3.3.10). The investigated device architectures, FTO/ZnO/$BaZrS_3$/Spiro-OMeTAD/Au, were analyzed by varying key parameters, including the thickness of the absorber layer, HTL, ETL, and FTO, within the range of 300 nm to 3000 nm. Similarly, the FTO/ZnO/$BaZrSe_3$/Spiro-OMeTAD/Au configuration was examined under the same conditions to evaluate its performance. Additionally, the impact of defect density ($10^{10} - 10^{17} cm^{-3}$) and operating temperature (300–450 K) was thoroughly examined. For $BaZrS_3$, a power conversion efficiency (PCE) of 13.45% was achieved at an absorber thickness of 3000 nm, with an open-circuit voltage (V_{oc}) of 0.803 V, a short-circuit current density (J_{sc}) of 21.41 mA/cm^2, and a fill factor (FF) of 78.24%. In contrast, $BaZrSe_3$ exhibited significantly superior performance, achieving V_{oc} of 0.676 V, J_{sc} of 46.19 mA/cm^2, FF of 82.85% and a remarkable PCE of 26.53% at a thickness of 900 nm. The results reveal the potential of $BaZrSe_3$ CPs as highly efficient and eco-friendly substitutes for conventional lead halide perovskites, unlocking new possibilities for sustainable solar cell technology.

Keywords: $BaZrS_3$, $BaZrSe_3$, Chalcogenide Perovskites, Solar Cells, SCAPS-1D

1 Introduction

The increasing global demand for energy has necessitated a transition from conventional fossil fuel-based energy sources to sustainable alternatives[1,2]. Among various renewable energy technologies, solar energy has emerged as a crucial solution for addressing energy crises and mitigating environmental concerns. Solar energy can be efficiently harnessed using photovoltaic (PV) and thermoelectric technologies, which convert solar radiation into electrical energy[3]. The efficiency of these technologies largely depends on the choice of materials, as their electrical, optical, and thermal properties play a significant role in determining their performance[4].

In recent years, perovskite materials have garnered significant attention due to their remarkable physical and chemical properties, including spin-dependent transport, high thermoelectric power, magnetic ordering, ferroelectric behavior, and superior optoelectronic characteristics[5,6]. The perovskite family is broadly classified into oxide, halide, and chalcogenide perovskites, each exhibiting unique structural and electronic properties[7-12]. While oxide & halide perovskites have demonstrated remarkable potential for solar energy applications, they suffer from inherent limitations. Oxide perovskites generally exhibit large bandgaps due to the high electronegativity of oxygen, restricting their absorption to the ultraviolet (UV) range[13]. Halide perovskites, despite their excellent optoelectronic properties and high-power conversion efficiencies (PCEs), are hindered by toxicity concerns due to their lead content and poor environmental stability, limiting their commercial viability[14, 15].

Chalcogenide perovskites (CPs), with the general formula ABX_3 (where A and B are metal cations, and X denotes a chalcogen element, which can be sulfur, selenium, or tellurium, have emerged as promising alternatives to oxide and halide perovskites for PV applications[16-18]. These materials exhibit several advantages, including high absorption coefficients, tunable bandgaps, enhanced thermal and moisture stability, and environmentally friendly compositions[19, 20]. Unlike oxide perovskites, which suffer from large

*Corresponding Author: (E-mail: nikhil.thakur7018@gmail.com)

bandgaps, CPs possess bandgaps that can be tailored to optimize solar absorption. Their covalent bonding enhances charge transport properties while minimizing recombination losses, making them highly desirable for solar cell applications. Recent theoretical and experimental studies have identified several CPs, such as $CaZrS_3$, $SrZrS_3$, $BaHfS_3$, and $SrHfS_3$, as promising candidates for PV and optoelectronic applications[12, 21-26]. Moreover, mixed chalcogenide perovskites, such as $BaZr(S,Se)_3$, exhibit tunable bandgaps and enhanced stability, making them attractive for use in next-generation tandem solar cells.

Among various CPs, $BaZrS_3$ has gained significant attention as a promising material for thin-film PV applications, attributed to its direct bandgap, ranging approximately between 1.70-1.90 eV, high absorption in the visible spectrum, and excellent thermal and chemical stability[13,27-29]. These properties make $BaZrS_3$ suitable for solar energy conversion, particularly in single-junction and tandem solar cells. The ability to fine-tune its optoelectronic properties has led researchers to explore $BaZr(S_{1-x}Se_x)_3$, where the partial substitution of sulfur with selenium results in improved light absorption characteristics and better charge transport. However, $BaZrS_3$'s bandgap, while suitable for some PV applications, remains slightly larger than the ideal range for maximizing solar energy absorption.

Recently, $BaZrSe_3$ has gained significant attention due to its narrower bandgap, which falls in the range of 1.00–1.45 eV, making it an excellent candidate for solar cell applications [30-34]. Unlike $BaZrS_3$, $BaZrSe_3$ exhibits stronger light absorption in the near-infrared region, which is highly beneficial for improving power conversion efficiency. However, there is some variability in reported bandgap values due to differences in computational methods and structural configurations. Using the HSE06 hybrid functional, Ong *et al.*[31] estimated a direct bandgap of 1.11 eV, while Korbel *et al.*[30] reported an indirect bandgap of 1.01 eV. Additionally, they identified a direct bandgap of 1.44 eV. For the needle-like structure, Alowa *et al.* [32] estimated bandgaps of 0.92 eV and for the orthorhombic structure, 1.28 eV, Huo *et al.* [33], on the other hand, utilized the PBE0 hybrid functional and derived a bandgap of 1.34 eV. These variations highlight the need for further experimental validation to establish the precise electronic properties of $BaZrSe_3$.

Despite their remarkable potential, several challenges remain in optimizing CPs for PV applications. Some CPs have relatively high bandgaps, which limit their absorption range, necessitating bandgap engineering strategies such as alloying, strain engineering, and external pressure application. Additionally, improvements in synthesis techniques, defect passivation, and device architecture are required to achieve PCEs comparable to those of halide perovskites. In addition to the absorber layer, the choice of electron transport layer (ETL) and hole transport layer (HTL) plays a critical role in determining device performance. ZnO is widely used as an ETL because of its exceptional electron mobility, broad bandgap, and excellent chemical stability, all of which contribute to effective charge transport and extraction. Spiro-OMeTAD has similarly been widely used as an HTL in perovskite and chalcogenide-based solar cells due to its high hole mobility and excellent energy level alignment with the absorber layer, facilitating efficient charge collection.

In this study, SCAPS-1D simulation software is employed to investigate the PV performance of $BaZrS_3$ and $BaZrSe_3$-based solar cells. SCAPS-1D is a widely used numerical tool for modelling solar cell structures, enabling the optimization of material parameters, layer thicknesses, and interface properties to enhance efficiency. Specifically, the impact of absorber layer thickness, HTL, ETL, FTO, defect density, and temperature variations on key PV parameters such as open-circuit voltage (V_{oc}), short-circuit current density (J_{sc}), fill factor (FF), and PCE is analyzed. The results obtained from SCAPS-1D simulations provide valuable insights for advancing the design and development of high-efficiency chalcogenide perovskite solar cells (PSCs), contributing to ongoing efforts to establish lead-free, stable, and efficient alternatives to conventional perovskite-based photovoltaics.

2 Methodology

This study utilized SCAPS-1D (version 3.3.10), a one-dimensional solar cell simulation software designed by the Department of Electronics and Information Systems at the University of Ghent, Belgium[35, 36]. SCAPS-1D has been developed to utilize the optical and electrical properties of the materials under investigation to analyze thin-film solar cells. Its user-friendly interface, advanced defect modeling capabilities, and ability to handle multilayered structures make it an ideal choice for investigating environmentally friendly chalcogenide-based PSCs.

SCAPS-1D functions by solving coupled differential equations numerically, including Poisson's equation and the electron and hole continuity equations. These equations form the mathematical foundation for analyzing the electrical behavior of PV devices:

$$\frac{d}{dx}\left(-\varepsilon(x)\frac{d\varphi}{dx}\right) = q\left[p\,(x) - n\,(x) + N_d^+\,(x) - N_a^-\,(x)\right] \quad \ldots (1)$$

Here, the parameters are defined as follows:

$\varepsilon(x)$: Material permittivity
φ: Electrostatic potential
q: Elementary charge
$p\,(x)$: Hole density
$n\,(x)$: Electron density
$N_d^+\,(x)$: Ionized donor concentration
$N_a^-\,(x)$: Ionized acceptor concentration

Electron Continuity Equation

$$\frac{\partial j_n}{\partial x} = q\left(R_n - G + \frac{\partial n}{\partial t}\right) \quad \ldots (2)$$

Hole Continuity Equation

$$\frac{\partial j_p}{\partial x} = -q\left(R_p - G + \frac{\partial p}{\partial t}\right) \quad \ldots (3)$$

In these equations:

- j_n : Electron current density
- j_p : Hole current density
- R_n : Net recombination rate for electrons per unit volume
- R_p : Net recombination rate for holes per unit volume
- G: Generation rate per unit volume

These equations are solved by SCAPS-1D to calculate important solar cell performance metrics including V_{oc}, J_{sc}, FF, and PCE. Moreover, it allows for an in-depth analysis of device performance by providing insights into recombination dynamics, charge generation, and defect influences.

2.1 Architecture of the Device

This study evaluates and compares the efficiency and performance of two different photovoltaic device architectures. The configurations of these solar cells are presented in Fig. 1 (a-b). Device 1 features the structure $FTO/ZnO/BaZrS_3/Spiro-OMeTAD/Au$, while Device 2 is composed of $FTO/ZnO/BaZrSe_3/Spiro-OMeTAD/Au$. Both devices are designed to optimize charge carrier transport, absorption, and collection to achieve high photovoltaic performance.

The transparent conducting oxide (TCO), which is composed of fluorine-doped tin oxide (FTO), serves as the outermost layer in both device configurations. FTO serves a dual purpose: it allows the efficient transmission of incident light to the active layer and acts as the front electrode for electron extraction. Its excellent optical transparency and low sheet resistance make it an ideal choice for photovoltaic applications. The TCO also forms a stable interface with the ETL, ensuring smooth charge transfer and minimal energy losses.

Directly below the TCO, the ETL plays a critical role in ensuring the efficient extraction and transport of photogene rated electrons from the light-absorbing layer to the external circuit[37]. ZnO is selected as the ETL material for its superior transparency, exceptional

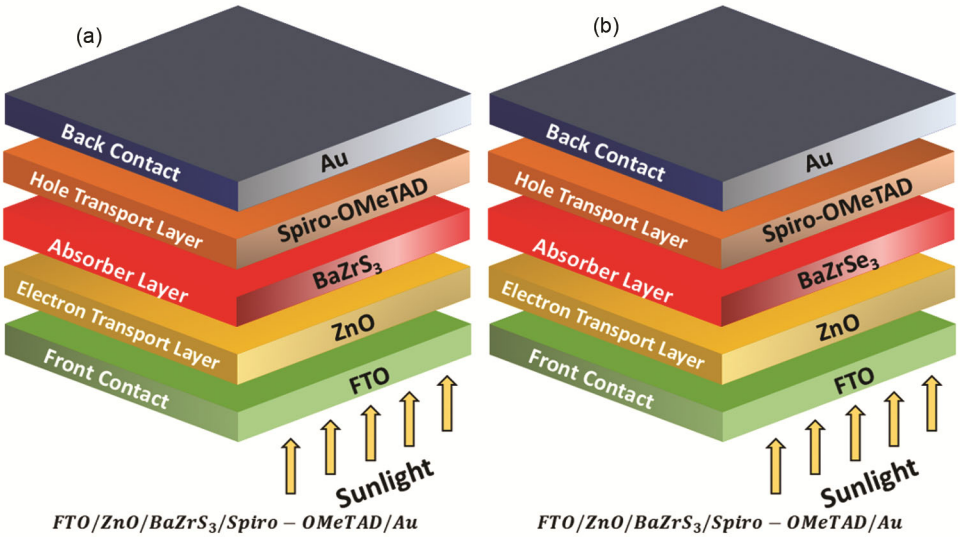

Fig. 1 — Solar cells configurations

electron mobility, and broad bandgap[38,39]. ZnO effectively reduces charge recombination by creating a favorable energy alignment for electron flow while blocking holes from the absorber layer. Its compatibility with scalable deposition techniques, such as sputtering, spray pyrolysis, and spin coating, makes it a versatile and cost-effective choice[40]. Additionally, ZnO contributes to suppressing charge accumulation at the interface, improving overall device stability.

The central component of both device structures is the light-absorbing layer, which determines the efficiency of sunlight absorption and the generation of charge carriers. In Device 1, the absorber layer consists of $BaZrS_3$, while $BaZrSe_3$ is used in Device 2. These chalcogenide perovskites are emerging as promising materials for PV applications owing to their high absorption coefficients, excellent thermal and chemical stability, and eco-friendly nature. $BaZrS_3$ exhibits a bandgap of approximately 1.70-1.80 eV[13, 27-29], whereas $BaZrSe_3$ has a slightly narrower bandgap (~1.01-1.44 eV)[30-34], allowing it to absorb a broader spectrum of sunlight. Both materials enable strong light-matter interaction, resulting in efficient photogeneration of electron-hole pairs. Above the absorber layer, the HTL facilitates the extraction and transport of photogenerated holes while blocking electrons. Spiro-OMeTAD is utilized as the HTL material in both devices. Spiro-OMeTAD is renowned for its high hole mobility, wide bandgap (~3 eV), and excellent chemical stability, making it an optimal choice for perovskite solar cells. Its compatibility with various perovskite absorbers and its ability to form a smooth interface with the metal contact contribute to efficient charge extraction and reduced interfacial losses. Additionally, Spiro-OMeTAD is less toxic and more cost-effective compared to alternative organic hole transport materials, enhancing the overall sustainability of the device.

The final layer in both device architectures is the metal back contact, responsible for collecting and transporting photogenerated charges to the external circuit. As a back contact, gold (Au) is chosen for its excellent electrical conductivity, chemical stability, and resistance to oxidation. Au ensures minimal energy loss during charge collection and provides long-term stability to the device. While other metals such as aluminium (Al), silver (Ag), or copper (Cu) could have been considered, Au was preferred because of its unmatched performance in maintaining consistent current flow and preventing degradation under operating conditions.

Both device architectures are optimized to maximize charge generation, separation, and collection. The combination of FTO, ZnO, chalcogenide perovskites ($BaZrS_3$ or $BaZrSe_3$), Spiro-OMeTAD, and gold creates a well-engineered stack that minimizes recombination losses, ensures efficient charge transport, and enhances overall PCE. The comparative performance analysis between $BaZrS_3$ and $BaZrSe_3$ highlights the impact of absorber material selection on device efficiency, light absorption, and charge carrier dynamics.

2.2 Simulated Parameters

Tables 1 and 2 include a predefined set of physical parameters that were used to start the simulation. These parameters were thoughtfully chosen, drawing from previous experimental and theoretical investigations, ensuring a high level of accuracy and reliability in our simulation results[41-54]. The parameters that correspond to the front and back contacts are shown in detail in Table 3.

Au was selected as the back contact material due to its exceptional properties, including impressive optical reflectivity and superior electrical conductivity. The

Table 1 — Essential input parameters for individual layers of the solar cell structure

Parameters	FTO (TCO)[26, 31]	ZnO (ETL)[48]	$BaZrS_3$ (Absorber)[30]	$BaZrSe_3$ (Absorber)[50, 55]	Spiro-OMeTAD (HTL)[44]
Thickness (nm)	400	600	200	200	150
Bandgap, E_g (eV)	3.50	3.20	1.70	1.01	2.90
Dielectric Permittivity	9.00	8.10	4.19	4.19	3.00
Electron Affinity (eV)	4.00	4.10	4.50	4.50	2.20
VB Effective Density of States (cm^{-3})	1.80×10^{19}	1.00×10^{18}	1.80×10^{19}	1.80×10^{19}	1.80×10^{19}
CB Effective Density of States (cm^{-3})	2.20×10^{18}	4.50×10^{18}	2.20×10^{18}	2.20×10^{18}	2.00×10^{18}
Hole Mobility ($cm^2V^{-1}s^{-1}$)	10	1	5.8	5.8	1.00×10^{-4}
Electron Mobility ($cm^2V^{-1}s^{-1}$)	20	300	11.30	11.30	1.00×10^{-4}
Shallow Uniform Acceptor Density, N_A (cm^{-3})	0	0	1.00×10^{17}	1.00×10^{17}	2.0×10^{19}
Shallow Uniform Donor Density, N_D (cm^{-3})	2.00×10^{19}	1.00×10^{20}	0	0	0
Total Defect Density (cm^{-3})	1.00×10^{15}	1.00×10^{14}	1.00×10^{14}	1.00×10^{14}	1.0×10^{14}

Table 2 — Interface defects included in the simulated model

Parameters	$ZnO/BaZrS_3$ & $ZnO/BaZrS_3$	$Spiro/BaZrS_3$ & $Spiro/BaZrSe_3$
Defect Type	neutral	neutral
Energetic Distribution	single	single
Holes Capture Cross Section (cm^2)	1.0×10^{-15}	1.0×10^{-16}
Electrons Capture Cross Section (cm^2)	1.0×10^{-15}	1.0×10^{-18}
Defect Energy Reference Level, E_t	above the maximum EV	above the maximum EV
Energy Level Relative to Reference (eV)	0.600	0.050
Total Defect Density (cm^{-2})	1.0×10^{11}	1.0×10^{8}

Table 3 — Summary of contact parameters, including work function and surface recombination velocities, for the device configuration

Contact Type	Parameters	Values	References
Front Contact	Metallic Work Function (eV)	4.40	[45, 48]
	Electron Recombination Velocity (cm/s)	1.0×10^7	
	Hole Recombination Velocity (cm/s)	1.0×10^7	
Back Contact	Metallic Work Function (eV)	5.10	[48, 56]
	Electron Recombination Velocity (cm/s)	1.0×10^7	
	Hole Recombination Velocity (cm/s)	1.0×10^7	

incorporation of gold plays a vital role in optimizing charge collection while also improving the device's light management capabilities. By reflecting photons back towards the absorber layer, gold plays a pivotal role in increasing the optical path length and enhancing photon absorption, ultimately improving the overall PV performance.

For consistency across all simulations, the temperature was maintained at 300 K, and the AM 1.5 G solar spectrum was used as the illumination source with a light intensity of 1000 W/m^2. Additionally, the electron and hole thermal velocities were uniformly set to 10^7 cm/s across all device layers to maintain consistency.

3 Results and Discussion

3.1 Role of Absorber Layer Thickness in Enhancing Solar Cell Performance

The efficiency of a solar cell is significantly impacted by the thickness of its absorber layer. While thicker absorbers generally enable greater photon capture and enhance the generation of charge carriers, there is a delicate balance to be maintained. If the absorber layer becomes too thick, it can restrict the movement of charge carriers, especially when their diffusion lengths are short, which can hamper efficient charge extraction[56]. On the other hand, if the layer is too thin, it may not absorb sufficient light, leading to reduced photocurrent and a drop in overall device performance. Additionally, excessive thickness can contribute to elevated recombination rates and increased series resistance, both of which adversely affect charge transport[57]. As such, determining the optimal absorber thickness is essential to unlock the maximum potential efficiency of the device, particularly under conditions free from material defects.

In this context, the $FTO/ZnO/BaZrS_3/Spiro-OMeTAD/Au$ structure, characterized by an absorber layer with a bandgap of 1.70 eV, V_{oc} exhibited a steady increase with the increasing thickness of the absorber layer. Starting at 0.767 V for a thickness of 300 nm, V_{oc} rose steadily to 0.803 V at 3000 nm, reflecting enhanced charge separation efficiency with increased thickness. The J_{sc} also displayed a significant upward trend, improving from 16.198 mA/cm^2 to 21.409 mA/cm^2, indicative of better photon absorption and carrier generation. While the FF saw a slight reduction from 79.16% to 78.24%, this minimal change suggests negligible resistive losses. Consequently, the PCE increased markedly, rising from 9.838% at 300 nm to a maximum value of 13.454% at 3000 nm, highlighting the enhanced performance achieved with thicker absorber layers in this design.

Alternatively, $FTO/ZnO/BaZrSe_3/Spiro-OMe-TAD/Au$, with an absorber layer exhibiting a bandgap of 1.01 eV, demonstrated a contrasting behavior. The V_{oc} decreased from 0.728 V at 300 nm to 0.676 V at 3000 nm, potentially due to higher recombination rates in thicker layers. In contrast, the J_{sc} improved significantly, growing from 39.903 mA/cm^2 to 46. 192 mA/cm^2, highlighting enhanced photon utilization and charge carrier generation with increasing thickness. The FF remained largely consistent, maintaining an average value of 82.850% for most thicknesses, with a minor decline to 82.650%

at 3000 nm. Notably, the PCE reached its highest value of 26.532% at 900 nm but gradually dropped to 25.814% at 3000 nm, driven by the reduction in V_{oc} and FF, even as J_{sc} continued to improve. These observed trends are illustrated in Fig. 2 (a-d).

3.2 Role of HTL Thickness in Enhancing Solar Cell Performance

For $FTO/ZnO/BaZrS_3/Spiro-OMeTAD/Au$, altering the HTL thickness within the range of 300 to 3000 nm had minimal impact on V_{oc}, which remained constant at 0.758 V. Similarly, J_{sc} exhibited negligible fluctuation, maintaining a steady value of approximately 13.567 mA/cm^2 across all thicknesses. However, a slight reduction in FF was observed, decreasing from 79.341% at 300 nm to 77.951% at 3000 nm, likely due to minor resistive losses associated with increased thickness. Consequently, the PCE showed a gradual decline from 8.157% to 8.014%, indicating that a thinner HTL is preferable for preserving efficiency in this configuration.

For $FTO/ZnO/BaZrSe_3/Spiro-OMeTAD/Au$, V_{oc} experienced only a slight variation, increasing marginally from 0.733 V at 300 nm to 0.734 V at 3000 nm. The J_{sc} remained stable at around 35.067 mA/cm^2 across all thicknesses, reflecting consistent carrier generation and transport. However, the FF decreased from 81.150% at 300 nm to 77.563% at 3000 nm. As a result, the PCE declined from 20.872% to 19.953%, indicating a minor efficiency drop with increased HTL thickness. These variations are illustrated in Fig. 3 (a-d).

3.3 Role of ETL Thickness in Enhancing Solar Cell Performance

For $FTO/ZnO/BaZrSe_3/Spiro-OMeTAD/Au$, increasing the ETL thickness from 300 nm to 3000 nm resulted in a slight reduction in V_{oc}, which started at 0.758 V and decreased to 0.756 V. Similarly, J_{sc} declined from 13.574 mA/cm^2 to 13.059 mA/cm^2, indicating a minor decrease in current generation efficiency as the ETL thickness increased. The FF remained relatively stable, fluctuating around 79.42%, suggesting that the impact on FF was minimal. Consequently, the PCE decreased from 8.168% at 300 nm to 7.842% at 3000 nm.

For configuration 4(b), V_{oc} remained unchanged at 0.733 V throughout the thickness range. However, J_{sc} showed a gradual decrease from 35.090 mA/cm^2 at 300 nm to 34.545 mA/cm^2 at 3000 nm, indicating a slight reduction in carrier collection efficiency with increasing ETL thickness. The FF remained nearly

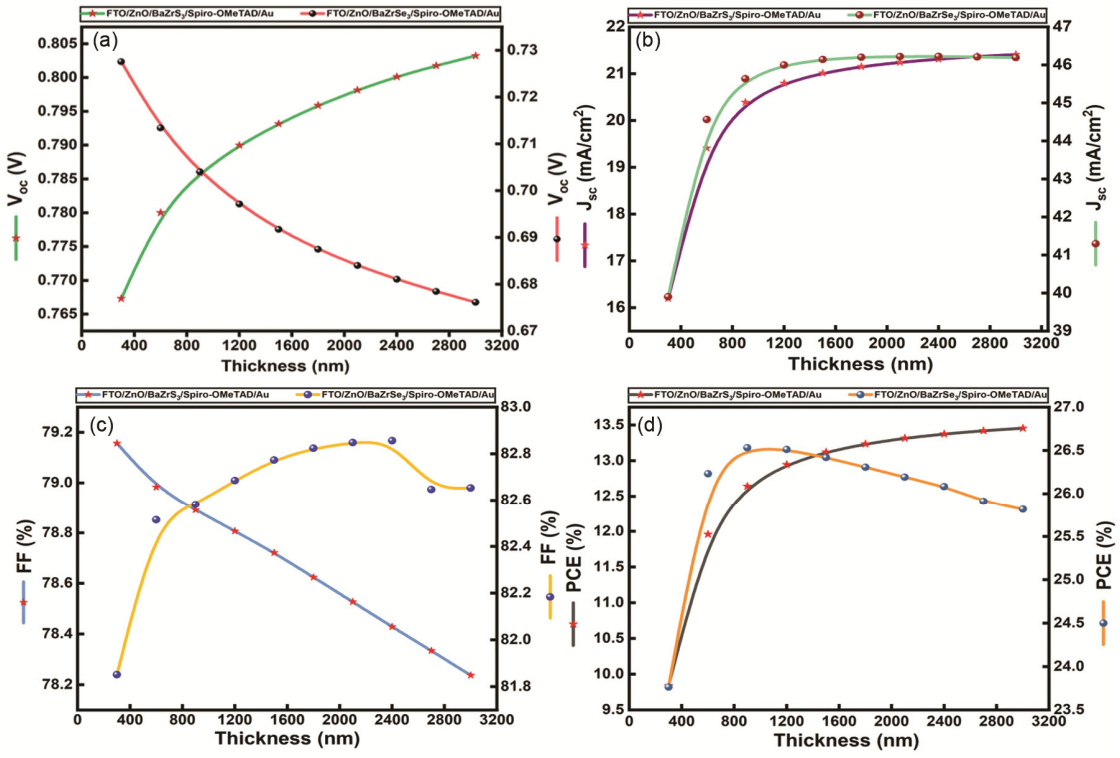

Fig. 2 — Influence of absorber layer thickness on V_{oc}, J_{sc}, FF, & PCE in the performance characteristics of ($BaZrS_3$, 1.70 eV) and ($BaZrSe_3$, 1.01 eV) solar cell structures

constant at approximately 81.35%, signifying negligible resistive losses. As a result, the PCE experienced a slight decline from 20.937% at 300 nm to 20.596% at 3000 nm, suggesting that thinner ETL layers are preferable for achieving optimal efficiency in this configuration. These trends are depicted in Fig. 4 (a-d).

3.4 Role of FTO Thickness in Enhancing Solar Cell Performance

For $FTO/ZnO/BaZrS_3/Spiro-OMeTAD/Au$, varying the FTO layer thickness from 300 nm to 3000 nm had a negligible impact on V_{oc}, which started at 0.758 V and slightly decreased to 0.757 V. A minor reduction was also observed in J_{sc}, which dropped from 13.591 mA/cm^2 to 13.375 mA/cm^2 as the thickness increased. The FF remained nearly unchanged at approximately 79.41%, indicating that the FTO thickness had little to no influence on fill factor. As a result, the PCE experienced a slight decline from 8.180% at 300 nm to 8.042% at 3000 nm, implying that a thinner FTO layer provides a marginally better device performance.

For $FTO/ZnO/BaZrSe_3/Spiro-OMeTAD/Au$, V_{oc} stayed constant at 0.733 V despite variations in absorber layer thickness between 300 and 3000 nm. A slight reduction in J_{sc} was noted, decreasing from 35.091 mA/cm^2 to 34.875 mA/cm^2, suggesting a minor decrease in carrier collection efficiency. The FF remained stable at approximately 81.35%, reflecting minimal impact on resistive losses. Consequently, the PCE showed a slight downward trend from 20.937% at 300 nm to 20.802% at 3000 nm. These variations are depicted in Fig. 5 (a-d).

3.5 Role of Defect Density in Determining Absorber Layer Performance

For $FTO/ZnO/BaZrS_3/Spiro-OMeTAD/Au$, the impact of defect density on solar cell performance is quite evident. At a lower defect density of $10^{10}cm^{-3}$, the device exhibits its best efficiency, achieving a PCE of 8.216%, alongside a V_{oc} of 0.759 V, J_{sc} of 13.586 mA/cm^2, as well as FF of 79.70%. As the defect density rises to $10^{14}cm^{-3}$, a small reduction in efficiency is observed, with PCE dropping to 8.165%, and corresponding decreases in V_{oc} (0.758 V), J_{sc} (13.568 mA/cm^2), and FF (79.41%). However, at $10^{16}cm^{-3}$, performance deteriorates significantly, leading to a sharp decline in

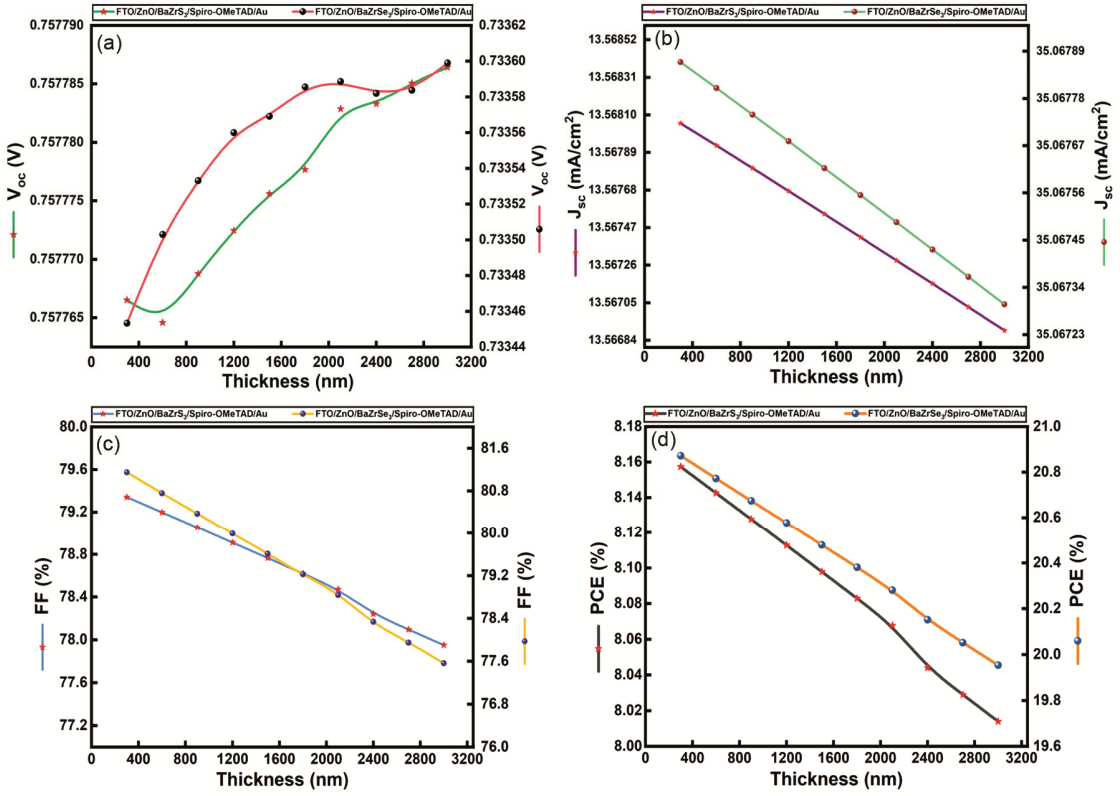

Fig. 3 — Influence of HTL thickness on V_{oc}, J_{sc}, FF, & PCE in the performance characteristics of ($BaZrS_3$, 1.70 eV) and ($BaZrSe_3$, 1.01 eV) solar cell structures

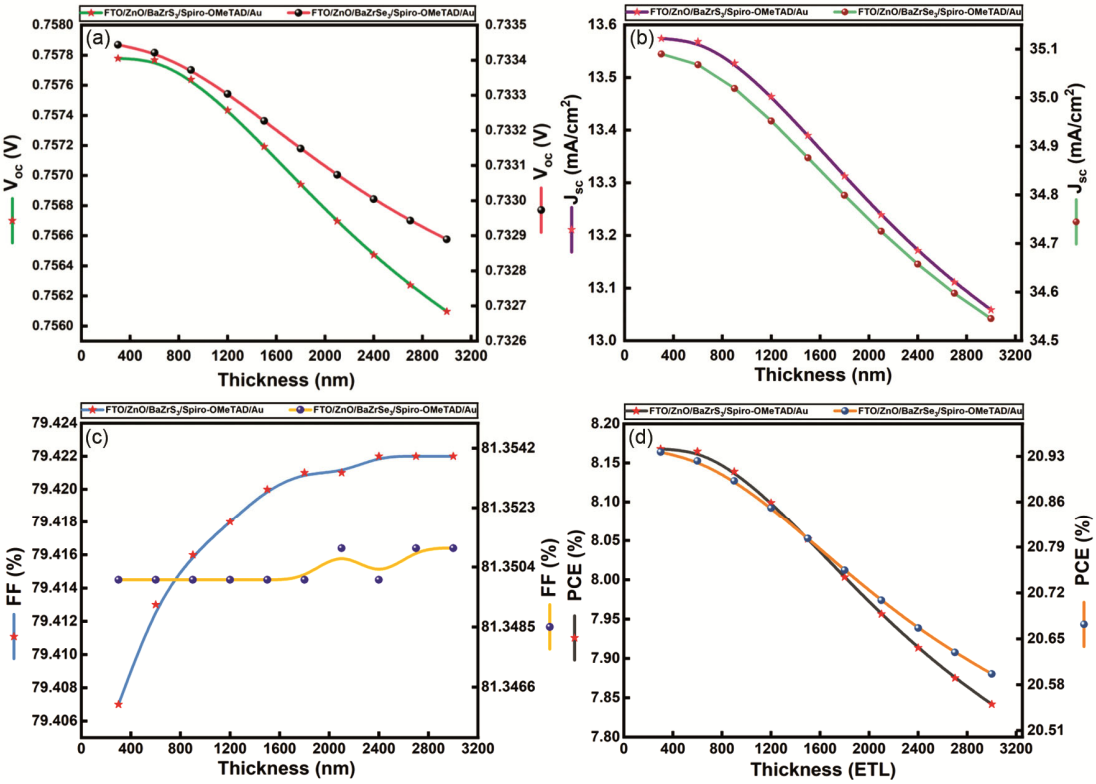

Fig. 4 — Influence of ETL thickness on V_{oc}, J_{sc}, FF, & PCE in the performance characteristics of ($BaZrS_3$, 1.70 eV) and ($BaZrSe_3$, 1.01 eV) solar cell structures

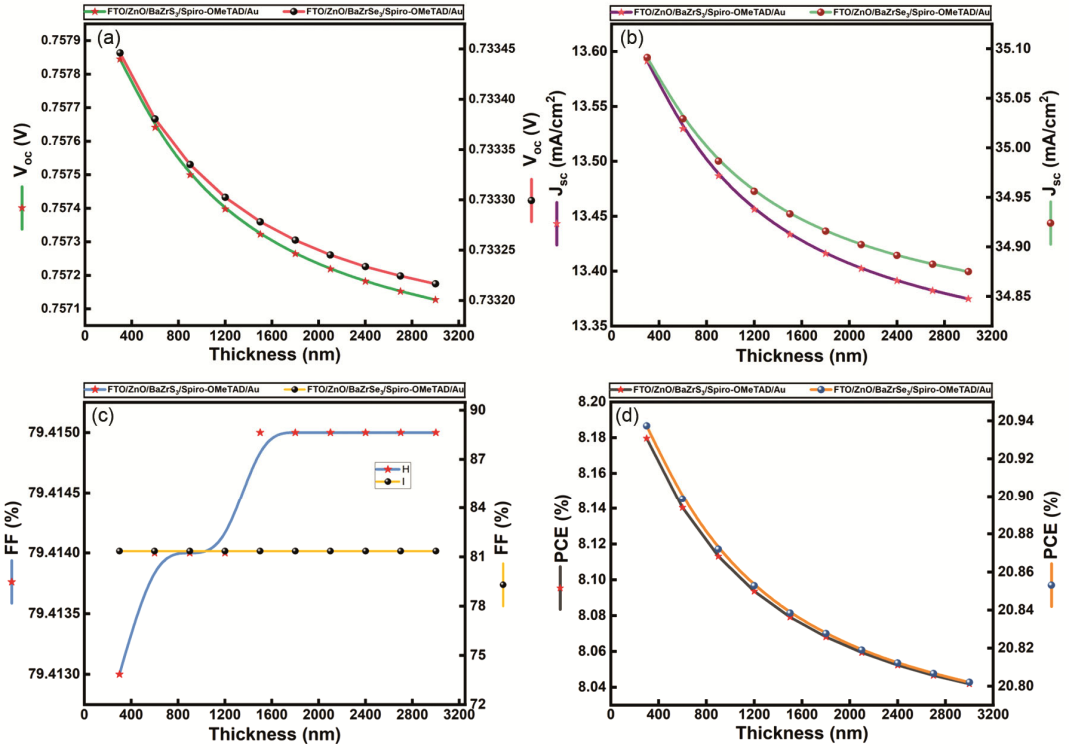

Fig. 5 — Influence of FTO thickness on V_{oc}, J_{sc}, FF, & PCE in the performance characteristics of ($BaZrS_3$, 1.70 eV) and ($BaZrSe_3$, 1.01 eV) solar cell structures

PCE to 6.024%, with V_{oc} decreasing to 0.713 V, J_{sc} reducing to 12.160 mA/cm^2, and FF dropping to 69.46%. At the highest defect density of $10^{17} cm^{-3}$, the efficiency dropped drastically to 3.767%, with further declines in V_{oc} (0.656 V), J_{sc} (9.796 mA/cm^2), and FF (58.597%).

Similarly, $FTO/ZnO/BaZrSe_3/Spiro-OMeTAD/Au$ follows the same pattern. At $10^{10} cm^{-3}$, the device achieves maximum efficiency, with a PCE of 22.359%, V_{oc} of 0.798 V, J_{sc} of 35.100 mA/cm^2, and FF of 79.84%. As the defect density increases to $10^{14} cm^{-3}$, the PCE drops slightly to 20.923%, while V_{oc} decreases to 0.733 V, J_{sc} remains nearly stable at 35.068 mA/cm^2, and FF is at 81.35%. A further increase in defect density to $10^{16} cm^{-3}$ leads to a substantial performance decline, reducing PCE to 14.235%, with V_{oc} dropping to 0.585 V, J_{sc} to 32.474 mA/cm^2, and FF to 74.94%. At the extreme defect density of $10^{17} cm^{-3}$, the PCE sees a reduction to 8.953%, with V_{oc} decreasing to 0.497 V, J_{sc} dropping to 26.821 mA/cm^2, and FF reducing to 67.167%.

These results clearly indicate that the presence of defects significantly impacts the performance of $BaZrS_3$ and $BaZrSe_3$ solar cells, emphasizing the critical need to minimize defects for achieving higher efficiencies. As defect density increases, the performance degradation is primarily due to enhanced non-radiative recombination facilitated by defect-assisted Shockley–Read–Hall (SRH) processes[58, 59]. Defects in the absorber layer introduce deep-level trap states within the bandgap, which serve as centers for carrier recombination. This results in a decrease in carrier lifetime, which leads to higher recombination losses[60]. Consequently, the increased recombination rate reduces the V_{oc} and FF, both of which are highly sensitive to recombination processes. For $BaZrSe_3$, which consistently exhibits superior efficiency across all defect densities, this indicates that its intrinsic material properties may help mitigate the effects of defects more effectively compared to $BaZrS_3$, making it a more promising candidate for high-performance PV applications. Figure 6 (a-d) illustrates these variations.

3.6 Analysis of Solar Cell Performance Under Varying Temperatures

The influence of temperature on the photovoltaic (PV) performance of the two perovskite solar cell configurations — $FTO/ZnO/BaZrS_3/Spiro-OMeTAD/Au$ *and* $FTO/ZnO/BaZrSe_3/Spiro-$

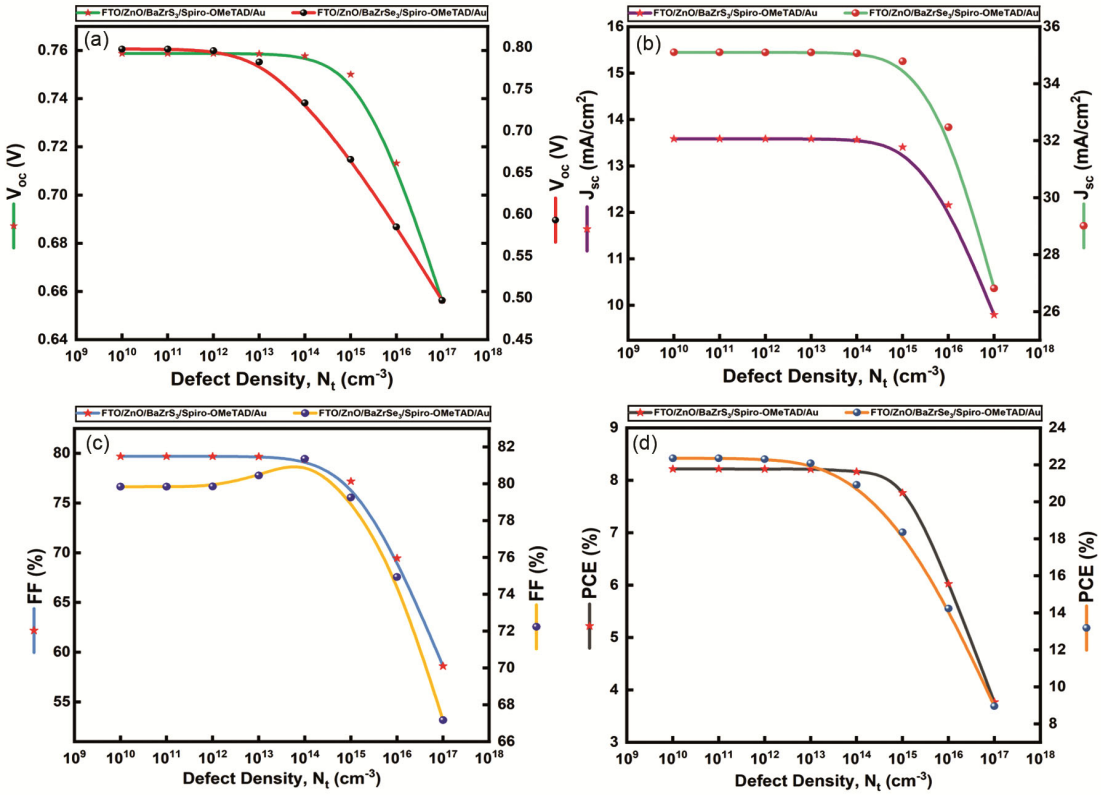

Fig. 6 — The impact of defect density on (a) V_{oc}, (b) J_{sc}, (c) FF, and (d) PCE is reflected in the performance characteristics of ($BaZrS_3$, 1.70 eV) and ($BaZrSe_3$, 1.01 eV) solar cell structures

$OMeTAD/Au$ — was systematically investigated in the temperature range of 300–450 K. The simulation results revealed a gradual degradation in key device parameters —particularly V_{oc} and FF— while the J_{sc} remained relatively stable with only minimal variations throughout the temperature range.

For the $BaZrS_3$-based device, as the temperature increased from 300 K to 450 K, the V_{oc} decreased from 0.675 V to 0.656 V, FF declined from 78.612% to 73.421%, and the PCE dropped from 6.740% to 6.198%, with J_{sc} showing a minor increase from 12.708 mA/cm^2 to 12.863 mA/cm^2. Similarly, for the $BaZrSe_3$-based device, V_{oc} reduced from 0.690 V to 0.547 V, FF decreased from 80.889% to 70.914%, and the PCE dropped significantly from 19.551% to 13.590%, whereas J_{sc} exhibited minimal variation, varying slightly from 35.007 mA/cm^2 to 35.015 mA/cm^2, indicating minimal impact of temperature on photocurrent generation.

This consistent decline in device performance with increasing temperature can be attributed to temperature-sensitive physical mechanisms in solar cells. The decrease in V_{oc} with temperature can be explained using the following relation[61, 62]:

$$\frac{d(V_{oc})}{dT} = \frac{V_{oc}}{T} - \frac{E_g/q}{T} \quad \ldots (4)$$

Here, $'E_g'$ is the bandgap energy of the absorber layer, $'q'$ is the elementary charge, and $'T'$ is the absolute temperature. As temperature rises, the reverse saturation current (I_0) increases exponentially due to enhanced thermal excitation of charge carriers. This leads to a reduction in V_{oc}, as the V_{oc} is logarithmically dependent on the photocurrent-to-dark current ratio.

Additionally, higher operating temperatures cause an increase in phonon activity, leading to enhanced non-radiative recombination and charge carrier scattering, which reduces both the FF and overall PCE. Although J_{sc} remains nearly stable due to stable light absorption, any slight changes are due to the reduced carrier mobility and diffusion lengths under thermal agitation[63].

The results from both $BaZrS_3$ and $BaZrSe_3$ devices clearly show that solar cell performance is temperature-sensitive, and thermal management is essential for maintaining long-term stability and efficiency in chalcogenide perovskite-based photovoltaics.

The detailed variations in V_{oc}, J_{sc}, FF, and PCE with temperature for both devices are presented in Fig. 7 (a–d).

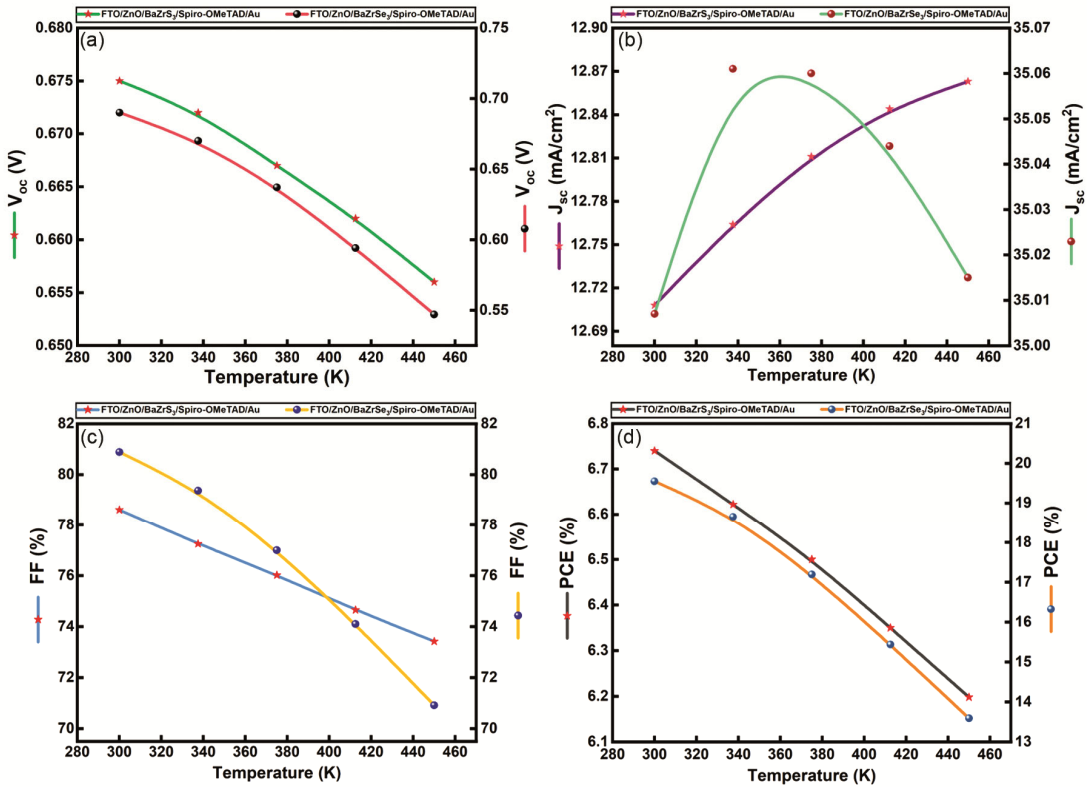

Fig. 7 — Influence of temperature on V_{oc}, J_{sc}, FF, & PCE in the performance characteristics of ($BaZrS_3$, 1.70 eV) and ($BaZrSe_3$, 1.01 eV) sola cell structures

4 Conclusion

This study comprehensively analyzed the performance of solar cells utilizing $BaZrSe_3$ and $BaZrS_3$ as absorber materials, focusing on the impact of absorber thickness, transport layers, defect density, and temperature variations. The results highlight the superior photovoltaic performance of $BaZrSe_3$ compared to $BaZrS_3$, positioning it as a more promising material for achieving high-efficiency solar cells. $BaZrS_3$-based devices demonstrated significantly PCE across various conditions. While both materials benefited from increasing absorber thickness, $BaZrSe_3$ achieved a peak efficiency of 26.532% at 900 nm, compared to $BaZrS_3$, which only reached 13.454% at 3000 nm. The higher J_{sc} of $BaZrSe_3$—rising from 39.903 mA/cm^2 to 46.192 mA/cm^2—indicates superior photon absorption and carrier generation due to its narrower bandgap (1.01 eV vs. 1.70 eV for $BaZrS_3$). Although V_{oc} showed a slight decrease with thickness, $BaZrSe_3$ still maintained a higher efficiency due to its remarkable charge carrier collection.

Variations in HTL and ETL thicknesses had minimal impact on V_{oc} and J_{sc}, but $BaZrSe_3$-based devices maintained higher overall efficiency across all thickness ranges. Even with increased HTL thickness, $BaZrSe_3$ maintained a high PCE of 19.953%, significantly outperforming $BaZrS_3$, which dropped to 8.014%. This suggests that $BaZrSe_3$ is less sensitive to variations in transport layers, making it more adaptable for practical device fabrication. Defect density analysis further established $BaZrSe_3$'s superiority. At an optimal defect density $10^{10} cm^{-3}$, $BaZrSe_3$ reached a remarkable efficiency of 22.359%, compared to 8.216% for $BaZrS_3$. Even at higher defect densities $10^{14} cm^{-3}$, $BaZrSe_3$ retained 20.923% efficiency, whereas $BaZrS_3$ dropped significantly to 8.165%. These results indicate that $BaZrSe_3$ exhibits stronger defect tolerance, making it more suitable for real-world applications where absolute material purity is difficult to achieve.

While both materials showed efficiency degradation with increasing temperature, $BaZrSe_3$ maintained a much higher performance across the temperature range. At 300 K, it exhibited 19.551% efficiency compared to 6.740% for $BaZrS_3$. Even at 450 K, $BaZrSe_3$ retained 13.590% efficiency, whereas $BaZrS_3$ dropped to 6.198%, demonstrating better thermal stability. This suggests that $BaZrSe_3$-based solar cells would be more resilient under varying environmental conditions.

Overall, $BaZrSe_3$ outperformed $BaZrS_3$ in all key performance metrics, including PCE, J_{sc}, defect tolerance, and temperature stability. Its exceptional efficiency, coupled with a broader absorption range and lower sensitivity to structural variations, makes it a highly promising material for next-generation photovoltaic applications. These findings emphasize the need for further research and optimization of $BaZrSe_3$-based solar cells to fully realize their potential for high-efficiency, stable, and scalable solar energy solutions.

References

1 Jana M K, Janke S M, Dirkes D J, Dovletgeldi S, Liu C, Qin X, Gundogdu K, You W, Blum V & Mitzi D B, *J Am Chem Soci*, 141 (19) (2019) 7955.
2 Yang J, Zhang P & Wei S-H, *J phys chem lett*, 9 (1) (2018) 31.
3 Xiao Z, Du K-Z, Meng W, Wang J, Mitzi D B & Yan Y, *J Am Chem Soci*, 139 (17) (2017) 6054.
4 Bhamu K, Soni A & Sahariya J, *Solar Energy*, 162 (2018) 336.
5 Zhou L, Xu Y F, Chen B X, Kuang D B & Su C Y, *Small*, 14 (11) (2018) 1703762.
6 Reshak A, Phys Chem Chem Phys, 16 (22) (2014) 10558.
7 Sopiha K V, Comparotto C, Márquez JA & Scragg J J, *Adv Opt Mater*, 10 (3) (2022) 2101704.
8 Hossain M K, Toki G I, Kuddus A, Rubel M, Hossain M, Bencherif H, Rahman M F, Islam M R & Mushtaq M, *Scientific Reports*, 13 (1) (2023) 2521.
9 Yuan M, Zhang X, Kong J, Zhou W, Zhou Z, Tian Q, Meng Y, Wu S & Kou D, *Electrochimica Acta*, 215 (2016) 374.
10 Rani U, Kamlesh P K, Joshi T K, Singh R, Al-Qaisi S, Gupta R, Kumar T & Verma A S, *J Mol Model*, 29 (10) (2023) 329.
11 Tiwari D, Hutter O S & Longo G, *J Phys Energy*, 3 (3) (2021) 034010.
12 Liang Y, Li J, Chen Z, Li G, Li M, Jia M, Chen X, Li X, Han Y & Shi Z, *Adv Opt Mater*, 12 (6) (2024) 2301977.
13 Ravi V K, Yu S H, Rajput P K, Nayak C, Bhattacharyya D, Chung D S & Nag A, *Nanoscale*, 13 (3) (2021) 1616.
14 Wu P, Wang S, Li X & Zhang F, *Matter*, 5 (4) (2022) 1137.
15 Wang M, Wang W, Ma B, Shen W, Liu L, Cao K, Chen S & Huang W, *Nano-Micro Letters*, 13 (1) (2021) 62.
16 Jess A, Yang R & Hages C J, *Chem Mater*, 34 (15) (2022) 6894.
17 Njema G G & Kibet J K, *Next Nanotechnol*, 7 (2025) 100102.
18 Samuel S M, Shaji S, Avellaneda D A & Krishnan B, *Nano Exp*, 6 (1) (2025) 015002.
19 Han Y, Fang X & Shi Z, *Appl Phys Rev*, 11 (2) (2024).
20 Chakravorty A, Adhikari S & Johari P, arXiv preprint arXiv:2502.14798, 2025.
21 Bareth B K & Tripathi M N, *Solar Energy Mater Solar Cells*, 282 (2025) 113445.
22 Basera P & Bhattacharya S, *J Phys Chem Lett*, 13 (28) (2022) 6439.
23 Han Y, Fang J, Liang Y, Gao H, Yang J, Chen X, Yuan Y & Shi Z, *Appl Phys Lett*, 124 (13) (2024).
24 Srinivasan D, Rasu Chettiar A D, Mercy E N V & Marasamy L, *Scientific Reports*, 15 (1) (2025) 3454.
25 Rahman M Z, Hasan S S, Akter M S, Rayhan M A, Hasan M Z & Islam M A, *MRS Advances*, 2024.

26 Eya H I, Ntsoenzok E & Dzade N Y, *Materials*, 13 (4) (2020) 978.
27 Comparotto C, Davydova A, Ericson T, Riekehr L, Moro M V, Kubart T & Scragg J, *ACS Appl Energy Mater*, 3 (3) (2020) 2762.
28 Perera S, Hui H, Zhao C, Xue H, Sun F, Deng C, Gross N, Milleville C, Xu X & Watson D F, *Nano Energy*, 22 (2016) 129.
29 Wei X, Hui H, Zhao C, Deng C, Han M, Yu Z, Sheng A, Roy P, Chen A & Lin J, *Nano Energy*, 68 (2020) 104317.
30 Körbel S, Marques M A & Botti S, *J Mater Chem C*, 4 (15) (2016) 3157.
31 Ong M, Guzman D M, Campbell Q, Dabo I & Jishi R A, *J Appl Phys*, 125 (23) 2019.
32 Alowa F, *Computational Study of the Thermoelectric Performance of Barium Chalcogenide Perovskites*, 2021.
33 Huo Z, Wei S H & Yin W J, *J Phys D: Appl Phys*, 51 (47) (2018) 474003.
34 Meng W, Saparov B, Hong F, Wang J, Mitzi D B & Yan Y, *Chem Mater*, 28 (3) (2016) 821.
35 Burgelman M, Nollet P & Degrave S, *Thin solid films*, 361 (2000) 527.
36 Burgelman M, Decock K, Niemegeers A, Verschraegen J & Degrave S, *SCAPS Manual, version 29*. University of Gent, 2016.
37 Abubaker S A & Pakhuruddin M Z, *Energy Technol*, 12 (9) (2024) 2400285.
38 El Ouakili S, Zahdi H, Laalioui S, Rajira A, Aqachmar Z, Abounadi A, Elhichou A, Almaggoussi A & Rochdi N, *Opt Mater*, 156 (2024) 115931.
39 Mahmud M A, Elumalai N K, Upama M B, Wang D, Chan K H, Wright M, Xu C, Haque F & Uddin A, *Solar Energy Materials and Solar Cells*, 159 (2017) 251.
40 Lv Y, Cai B, Yuan R, Wu Y, Qiao Q, & Zhang W H, *J Energy Chem*, 82 (2023) 66.
41 Du H J, Wang W C & Zhu J Z, *Chinese Phys B*, 25 (10) (2016) 108802.
42 Karthick S, Bouclé J & Velumani S, *Solar Energy*, 218 (2021) 157.
43 Alla M, Manjunath V, Chawki N, Singh D, Yadav S C, Rouchdi M & Boubker F, *Opt Mater*, 124 (2022) 112044.
44 Karthick S, Velumani S & Bouclé J, *Solar Energy*, 205 (2020) 349.
45 Helander M G, Greiner M, Wang Z, Tang W M & Lu Z, *J Vac Sci & Technol A*, 29 (1) 2011.
46 De Los Santos I M, Cortina-Marrero H J, Ruíz-Sánchez M, Hechavarría-Difur L, Sánchez-Rodríguez F, Courel M & Hu H, *Solar Energy*, 199 (2020) 198.
47 Azri F, Meftah A, Sengouga N & Meftah A, *Solar Energy*, 181 (2019) 372.
48 Chawki N, Rouchdi M, Alla M & Fares B, *Solar Energy*, 262 (2023) 111913.
49 Hossain, M K, Samajdar D, Das R C, Arnab A, Rahman M F, Rubel M, Islam M R, Bencherif H, Pandey R & Madan J, *Energy & Fuels*, 37 (5) (2023) 3957.
50 Thakur N, Kumar P, Neffati R & Sharma P, *Physica Scripta*, 98 (6) (2023) 065921.
51 Thakur N, Kumar P & Sharma P, *Materials Today: Proceedings*, 2023.
52 Karthick S, Nwakanma O M, Mercyrani B, Boucle J & Velumani S, *Adv Theory Simul*, 4 (11) (2021) 2100121.
53 Hussain S S, Riaz S, Nowsherwan G A, Jahangir K, Raza A, Iqbal M J, Sadiq I, Hussain S M & Naseem S, *J Renew Energy*, 2021 (2021) 1.
54 Hossain M I, Alharbi F H & Tabet N, *Solar Energy*, 120 (2015) 370.
55 Aly K, Thakur N, Kumar P, Saddeek Y, Shater T, Ismail Y A & Sharma P , *Solar Energy*, 282 (2024) 112961.
56 Karthick S, Velumani S & Bouclé J, *Opt Mater*, 126 (2022) 112250.
57 Yasin S, Al Zoubi T & Moustafa M, *Optik*, 229 (2021) 166258.
58 Green M A, *Solid-State Electron*, 24 (8) 1981 788.
59 Shockley W & Queisser H J, *J Appl Phys*, 32 (3) (1961) 510.
60 Tress W, *Adv Energy Mater*, 7 (14) (2017) 1602358.
61 Et-taya L, Ouslimane T, & Benami A, *Solar Energy*, 201 (2020) 827.
62 Green M A, Progress in Photovoltaics: Research and Applications, 11 (5) (2003) 333.
63 Khattak Y H, Baig F, Ullah S, Mari B, Beg S & Ullah H, *J Renew Sustain Energy*, 10 (3) 2018.